Water−Gas Shift Reaction on Metal Nanoclusters Encapsulated in Mesoporous Ceria Studied with Ambient-Pressure X-ray Photoelectron Spectroscopy

Cun Wen,[†,§] Yuan Zhu,[†,§] Yingchun Ye,[†,§] Shiran Zhang,[†] Fang Cheng,[†] Yi Liu,[†] Paul Wang,[‡] and Franklin (Feng) Tao[†,*]

[†]Department of Chemistry and Biochemistry, University of Notre Dame, Notre Dame, Indiana 46556, United States and [‡]Department of Physics, Bradley University, Peoria, Illinois 61625, United States. [§]These authors contributed equally.

Mesoporous materials have attracted much interest since MCM-41 was discovered in 1992.[1,2] As a result of intense research efforts, a broad spectrum of mesoporous materials have been synthesized, ranging from silica to metal oxides.[3−6] Currently, the affluent mesoporous materials are playing key roles in many fields, such as the fuel production and environmental protection, which fully benefit from the unique properties of the mesoporous materials.[7,8]

One property of the mesoporous materials under intensive studies is the confinement effect, which is due to the small physical size of the pores. The spatial confinement of the nanoscale channel in mesoporous materials creates spatial selectivity between two reactants or between the reactant and active sites.[9−11] For instance, the enantiomeric excess (ee) value in the epoxidation of non-functionalized olefins on mesoporous Mn catalysts increases with decreasing pore size because the small pores could enhance spatial recognition.[12] Recent studies showed that Fe catalysts encapsulated in carbon nanotubes (CNTs), whose pore sizes are similar to mesoporous material, have an enhanced catalytic activity in Fischer−Tropsch synthesis (FTS).[13−15] There was some peculiar interaction between the catalyst nanoclusters and the inner wall of the CNT resulting from electron transfer driven by a difference in electron density between the external surface and internal wall of a CNT. For catalysis in CO hydrogenation, this unique interaction could promote the CO dissociation to accelerate the overall reaction rate of FTS.

ABSTRACT
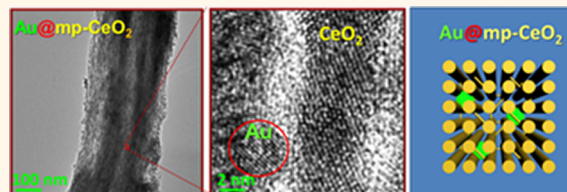
Metal nanoclusters (Au, Pt, Pd, Cu) encapsulated in channels of mesoporous ceria (*mp*-CeO₂) were synthesized. The activation energies of water−gas shift (WGS) reaction performed at oxide−metal interfaces of metal nanoclusters encapsulated in *mp*-CeO₂ (M@*mp*-CeO₂) are lower than those of metal nanoclusters impregnated on ceria nanorods (M/rod-CeO₂). *In situ* studies using ambient-pressure XPS (AP-XPS) suggested that the surface chemistry of the internal concave surface of CeO₂ pores of M@*mp*-CeO₂ is different from that of external surfaces of CeO₂ of M/rod-CeO₂ under reaction conditions. AP-XPS identified the metallic state of the metal nanoclusters of these WGS catalysts (M@*mp*-CeO₂ and M/rod-CeO₂) under a WGS reaction condition. The lower activation energy of M@*mp*-CeO₂ in contrast to M/rod-CeO₂ is related to the different surface chemistry of the two types of CeO₂ under the same reaction condition.

KEYWORDS: catalysis · water−gas shift · ambient-pressure X-ray photoelectron spectroscopy · ceria · *in situ*

However, mesoporous materials still lack fundamental studies toward understanding the enhancement of catalytic performances from the point of view of the surface chemistry of the internal concave surface of pores of mesoporous materials. For example, a concave internal surface could potentially increase the repulsion of adsorbates or intermediates formed during catalysis related to the limited concave surface. This effect on a catalytic reaction, which involves the participation of the internal surface of porous
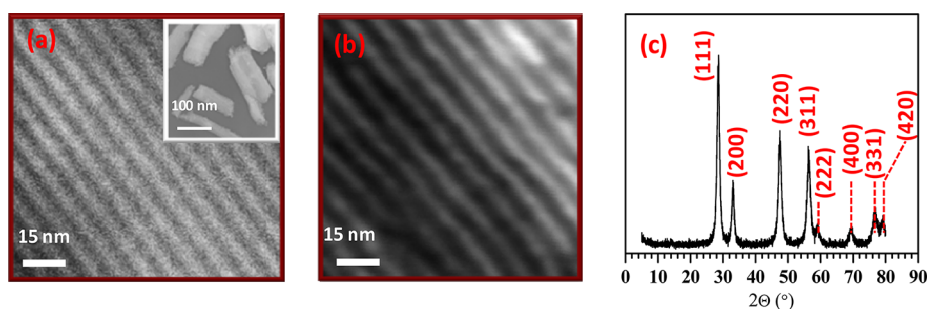
Figure 1. SEM images of SBA-15 (a) and *mp*-CeO$_2$ (b), and XRD pattern of the synthesized *mp*-CeO$_2$ (c).

particles, is expected to be greater than catalysis in which an inert support such as silica is not involved. Herein, we bring forward a fundamental study to understand the role of an *internal* concave surface of reducible oxide such as *mp*-CeO$_2$. Rod-CeO$_2$ with an external open surface was used for comparison.

The chosen reaction to examine the role of the internal concave surface is the water−gas shift (WGS) reaction. One reason is that CeO$_2$ is one of the active components of this reaction.[16] It is well acknowledged that the oxygen vacancies dissociate H$_2$O molecules and thus provide an OH group for coupling between an OH group and an adsorbed CO molecule to form an intermediate toward dissociation and a following formation of CO$_2$.[16−18] Another reason that the effort to understand the catalytic mechanism of the WGS on metal−oxide bifunctional catalysts, mostly called low-temperature WGS catalysts, is ongoing[17,19−25] as an active, robust low-temperature WGS catalyst is critical for on-site purification of H$_2$ source in the large-scale applications of low-temperature fuel cell technology. Au, Pt, Pd, and Cu are chosen to study since they are active for WGS, and nanoclusters of these metals supported on oxide were well studied.

We synthesized metal nanoclusters supported on internal concave surfaces of CeO$_2$ pores of *mp*-CeO$_2$ and the external surface of rod-CeO$_2$. One of the key factors in understanding heterogeneous catalysis is the surface chemistry of the active phase during catalysis. It is well acknowledged that surface chemistry of an active phase of catalysis is determined by reaction conditions.[26−30] Thus, an exploration of surface chemistry of catalysts under reaction conditions through *in situ* studies is significant for understanding the catalytic mechanism. Here we used ambient-pressure XPS technique[31−33] to track the surface chemistry of catalysts during catalysis (in the presence of reactant gases at reaction temperatures).

Kinetic studies suggested lower activation energy of M@*mp*-CeO$_2$ than that of M/rod-CeO$_2$. AP-XPS studies showed that the internal concave surface of CeO$_2$ pores of *mp*-CeO$_2$ of M@*mp*-CeO$_2$ has a higher concentration of oxygen vacancies under a WGS reaction condition than the external CeO$_2$ surface of M/rod-CeO$_2$. A correlation between the surface chemistry of

catalysts and the corresponding catalytic properties was built. Higher concentration of oxygen vacancies of *mp*-CeO$_2$ in contrast to rod-CeO$_2$ under WGS reaction conditions probably results from a low adsorption energy of OH groups on the internal concave surface of pores of *mp*-CeO$_2$ due to the enhanced inter-adsorbate repulsion on the bent internal surface of *mp*-CeO$_2$.

RESULTS AND DISCUSSION

The template of *mp*-CeO$_2$, SBA-15, was synthesized and is shown in Figure 1a. Figure 1b is the SEM image of *mp*-CeO$_2$ prepared with the synthesized SBA-15. XRD patterns clearly show the crystallization of *mp*-CeO$_2$ (Figure 1c). The impregnation of metal nanoclusters in the internal wall of channels of *mp*-CeO$_2$ was performed. Pore size of *mp*-CeO$_2$ does not change upon the encapsulation of metal nanoclusters. Figure 2 presents TEM images of Au@*mp*-CeO$_2$ and Pt@*mp*-CeO$_2$. The lattice fringes of the metal nanoclusters were clearly identifiable and are shown in Figure 2a2,b2. For comparison, high-resolution TEM images of Au/rod-CeO$_2$ and Pt/rod-CeO$_2$ are presented in Figure 3a,b. TEM images of other catalysts are presented in Figures S5 and S6 in Supporting Information. Table 1 lists the average size of metal nanoclusters encapsulated in *mp*-CeO$_2$ and supported on rod-CeO$_2$. As the pores of *mp*-CeO$_2$ encapsulating different metal clusters are similar, the average sizes of Au, Pt, Pd, and Cu in *mp*-CeO$_2$ are very similar, 3−6 nm. Compared to the size of nanoclusters encapsulated in *mp*-CeO$_2$, metal nanoclusters deposited on rod-CeO$_2$ have a size of 4−6 nm. Thus, there is no significant difference between the size of metal nanoclusters in *mp*-CeO$_2$ and those on rod-CeO$_2$.

As shown in Figure 4, activation energies of WGS on *mp*-CeO$_2$ supported catalysts Pt@*mp*-CeO$_2$, Cu@*mp*-CeO$_2$, Pd@*mp*-CeO$_2$, and Au@*mp*-CeO$_2$ are lower than those on metal nanoclusters supported on surfaces of rod-CeO$_2$. For Pt@*mp*-CeO$_2$, the activation energy is ∼60 kJ mol^{-1}, lower than ∼78 kJ mol^{-1} for Pt/rod-CeO$_2$. The measured ∼78 kJ mol^{-1} is consistent with 74.8 kJ mol^{-1} reported in the literature.[17] A similar difference was observed on Cu@*mp*-CeO$_2$ (24 kJ mol^{-1}) and Cu/rod-CeO$_2$ (39 kJ mol^{-1}) (Figure 4). The measured activation energies of WGS on Cu/rod-CeO$_2$ are consistent
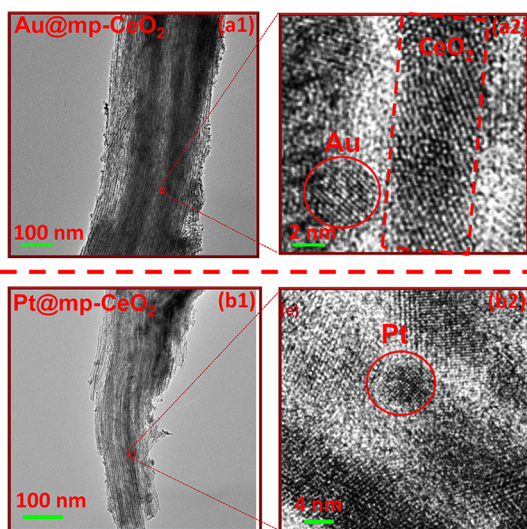
Figure 2. TEM images of the synthesized Au@*mp*-CeO$_2$ and Pt-@*mp*-CeO$_2$. (a1) Large-scale image of Au@*mp*-CeO$_2$; (a2) high-resolution image of Au@*mp*-CeO$_2$ showing the encapsulation of Au nanoclusters; (b1) large-scale image of Pt@*mp*-CeO$_2$; (b2) high-resolution image showing the encapsulation of Pt nanoclusters.
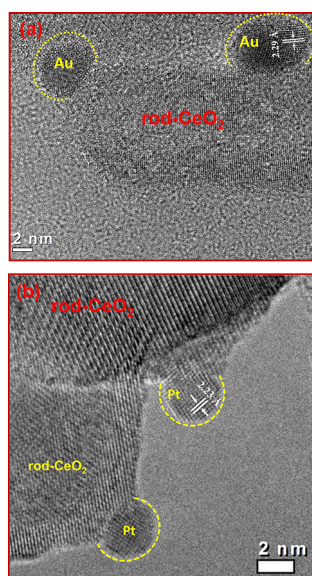

Figure 3. High-resolution TEM images of Au nanoclusters on rod-CeO$_2$ (a) and Pt nanoclusters on rod-CeO$_2$ (b).

with other reports such as 36 kJ mol^{-1} for Cu on CeO$_2$ in ref 21. The low activation energies of WGS on other catalysts encapsulated in *mp*-CeO$_2$ including Au@*mp*-CeO$_2$ and Pd@*mp*-CeO$_2$ were revealed, as well. The activation energy of WGS on Au@*mp*-CeO$_2$ is 11 kJ mol^{-1}, in contrast to 51 kJ mol^{-1} of Au/rod-CeO$_2$.[34] It is 34 kJ mol^{-1} on Pd@*mp*-CeO$_2$ in contrast to 76 kJ mol^{-1} on Pd nanoclusters supported on rod-CeO$_2$ and nanoparticles.[35]

To exclude a potential mass transfer limit in the kinetic studies of WGS, kinetic studies of M@*mp*-CeO$_2$ by changing the flow rate of reactants were performed. No dependence of measured activation energy on

TABLE 1. Sizes of Metal Nanoclusters Encapsulated in *mp*-CeO$_2$ and Supported on Rod-CeO$_2$

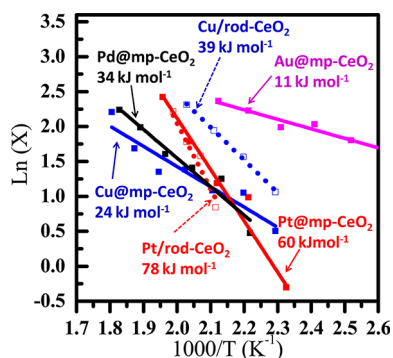| metal	support	average size (nm)
Au	*mp*-CeO$_2$	4 ± 1
Au	rod-CeO$_2$	4.5 ± 1.5
Pt	*mp*-CeO$_2$	4 ± 1
Pt	rod-CeO$_2$	4 ± 1
Pd	*mp*-CeO$_2$	4 ± 1.5
Pd	rod-CeO$_2$	5 ± 1.5
Cu	*mp*-CeO$_2$	4 ± 1
Cu	rod-CeO$_2$	4.5 ± 2

Figure 4. Arrhenius plot of WGS rates on metal nanoclusters supported on *mp*-CeO$_2$ and rod-CeO$_2$. Reaction condition and metal loading are the same for these catalysts. The reaction condition is fully described in the Methods section.

flowing rates was found. In addition, the potential influence of mass diffusion limit in the channels of *mp*-CeO$_2$ of M@*mp*-CeO$_2$ was tested by measuring the catalytic activity of catalyst particles of metal@*mp*-CeO$_2$ with different lengths between 100 nm and 10 μm. Catalyst activity would change with the length of the pore of *mp*-CeO$_2$ if mass transfer could be limited by an internal diffusion. However, our results showed that activities of these catalysts were very similar, although their particle sizes (essentially length of *mp*-CeO$_2$ particles) are different. This indicates that the influence of the internal diffusion on the catalyst activity is negligible. In addition, if the decrease of activation energies of M@*mp*-CeO$_2$ compared to those of M/rod-CeO$_2$ for the WGS reaction could result from a potential mass transfer limitation instead of an intrinsic property of the *mp*-CeO$_2$, activation energy of catalytic reactions such as CO oxidation performed on metal nanoclusters such as Pt encapsulated in an insert mesoporous material such as SBA-15 should be lower than that of Pt nanoparticles simply supported on silica particles. In fact, the measured activity energy of CO oxidation on Pt nanoclusters (2−7 nm) encapsulated in SBA-15 is similar to that of Pt on SiO$_2$ particles.[36] Thus, there is no mass transfer limitation for catalytic reaction performed in the M/*mp*-CeO$_2$.

The low WGS activation energies in the case of M@*mp*-CeO$_2$ catalysts in contrast to M/rod-CeO$_2$ indicate

a unique structure of the internal concave surfaces of the CeO_2 pores of *mp*-CeO_2. X-ray diffraction (XRD) patterns show that both *mp*-CeO_2 and rod-CeO_2 have face-centered cubic crystal structure (fcc, *Fm*3*m*, JCPDS 34-0394) (Figures 1c and S3a). It is expected that there is a strong metal support interaction between metal nanoclusters and CeO_2 as reported in the literature.[18,37,38] The strong interaction between the support and metal could weaken the neighboring Ce−O bond and thus modify the mobility of oxygen atoms.[37] The interaction between metal atoms and the local interface of *mp*-CeO_2 is similar to the interaction between metal atoms and the local interface of rod-CeO_2. Thus, we expect the strong metal−oxide interaction to play a similar role for metal nanoclusters on *mp*-CeO_2 and rod-CeO_2. Alternatively, the confinement effect of *mp*-CeO_2 is probably the main reason for the difference in catalytic properties.

Although *mp*-CeO_2 and rod-CeO_2 have a similar crystal structure, the surfaces of *mp*-CeO_2 and rod-CeO_2 are different. The scanning transmission electron microscopy (STEM) images indicated that the *mp*-CeO_2 has a well-defined mesoporous structure replicated from SBA-15 (Figure 1a,b). The *mp*-CeO_2 has an internal concave surface of CeO_2 pores of *mp*-CeO_2 different from the external surface of rod-CeO_2. This internal concave surface of the CeO_2 pore of *mp*-CeO_2 is also different from the external surface of a whole *mp*-CeO_2 particle.[39] The TEM images of Au@*mp*-CeO_2 and Pt@*mp*-CeO_2 show that the metal nanoclusters are *encapsulated in* the *mp*-CeO_2 (Figure 2). This is different from the metal nanoclusters *impregnated on* the external surface of a *mp*-CeO_2 particle. Our catalytic measurements showed that the internal concave surface of the CeO_2 pores of *mp*-CeO_2 could be important for the WGS and thus reduce the activation energy. Thus the different surface structure of the internal concave surface of CeO_2 pores of *mp*-CeO_2 could result in different catalytic behaviors.

To build a correlation between the measured difference in activation energies and the potential difference in surface chemistry of different CeO_2, we performed *in situ* studies of these catalysts by using AP-XPS in reduction with H_2 at 300 °C or under WGS reaction conditions: Au@mp-CeO_2, Pt@mp-CeO_2, Cu@mp-CeO_2, Pd@mp-CeO_2, Au/rod-CeO_2, Pt/rod-CeO_2, Cu/rod-CeO_2, and Pd/rod-CeO_2.

Figures 5−8 present the photoemission features of Au and Pt nanoclusters encapsulated in channels of *mp*-CeO_2 and supported on rod-CeO_2 catalysts *during* WGS. As described in the Methods section, XPS studies of M@*mp*-CeO_2 were performed on samples upon Ar sputtering. The same photoemission features of core levels of metals were observed upon sputterings of different amounts of time. It suggested that the metal nanoclusters were certainly encapsulated in CeO_2 pores of *mp*-CeO_2 (Figure S3c). Otherwise, there would not be photoemission features of core levels of metal
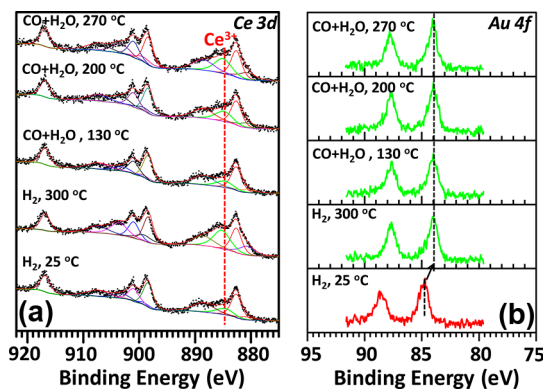

Figure 5. Photoemission features of (a) Ce 3d and (b) Au 4f of Au@*mp*-CeO_2 under reaction conditions studied with AP-XPS. P_{CO} = 0.3 Torr, P_{H_2O} = 1.2 Torr, P_{H_2} = 1 Torr. Reaction temperatures are given in the figure.
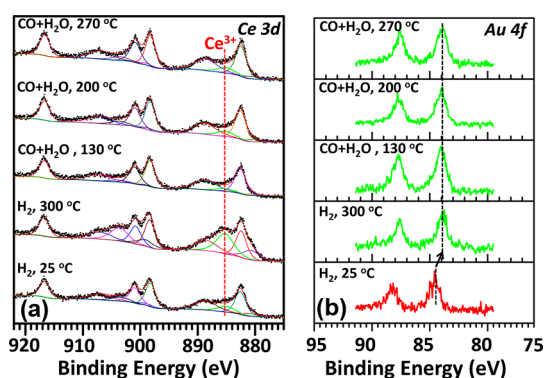

Figure 6. Photoemission features of (a) Ce 3d and (b) Au 4f of Au/rod-CeO_2 under reaction conditions studied with AP-XPS. P_{CO} = 0.3 Torr, P_{H_2O} = 1.2 Torr, P_{H_2} = 1 Torr. Reaction temperatures are given in the figure.
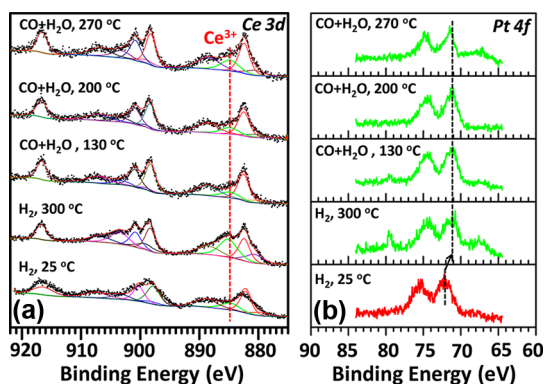

Figure 7. Photoemission features of (a) Ce 3d and (b) Pt 4f of Pt@*mp*-CeO_2 under reaction conditions studied with AP-XPS. P_{CO} = 0.3 Torr, P_{H_2O} = 1.2 Torr, P_{H_2} = 1 Torr. Reaction temperatures are given in the figure.

nanoclusters after removal of a certain shell region of M@*mp*-CeO_2 through sputtering (Figure S3).

Spectra of Ce 3d of the eight catalysts under reaction conditions are listed in Figures 5a, 7a, 8a, 9a, S7, S8, S9, and S10. Typically, a Ce 3d spectrum can be deconvoluted into photoemission features of Ce^{3+} and Ce^{4+}.[40]

Due to a final state effect, there are five sets of 3d spin−orbit split doublets. The peaks denoted by u‴, u″, u, v‴, v″, and v are attributable to Ce^{4+}, which are dominant in these catalysts (Figures 5−8 and S7−S10). Meanwhile, the u′, u^0, v′, and v^0 peaks are assigned to Ce^{3+}. For all of the Ce 3d spectra, the same constraint was implemented during their deconvolutions. The peak positions and widths of these components in different spectra strictly remained consistent. For each spin−orbital splitting, the energy split remained constant for catalysts with different support (mp-CeO_2 or rod-CeO_2). The implementation of these identical parameters makes the comparison of calculated Ce^{3+} atomic fractions of different spectra collected under different reaction conditions eligible.

The evolution of oxygen vacancy density presented by Ce^{3+} fractions in Figure 9 suggests a different surface chemistry of internal concave walls of the CeO_2 pore of mp-CeO_2 of M@mp-CeO_2 in contrast to the external surface of rod-CeO_2 of M/rod-CeO_2 under the same reaction condition. For example, the fraction of Ce^{3+} in M@mp-CeO_2 under a WGS condition is typically 17−28% or even larger. However, it is about 4−12% in the case of M/rod-CeO_2 under the same WGS condition. A similar difference was exhibited between

Pd@mp-CeO_2 and Pd/rod-CeO_2 and between Cu@mp-CeO_2 and Cu/rod-CeO_2, as well.

The fraction of Ce^{3+} in Au@mp-CeO_2 and Pt@mp-CeO_2 is ∼17 and ∼16% before a WGS reaction (Figure 9). Upon a treatment of H_2 at 300 °C, density of oxygen vacancies (represented with the fraction of Ce^{3+} in the total of Ce^{3+} and Ce^{4+}) increases to ∼39% (measured in the presence of H_2 at 300 °C). During WGS catalysis, however, the density of oxygen vacancies remains at 18−28% for Au@mp-CeO_2 and 16−27% for Pt@mp-CeO_2. It is suggested that H_2O dissociatively adsorbs on oxygen vacancies, decreasing density of oxygen vacancies created in the H_2 pretreatment. Under the WGS reaction condition, the Ce^{3+} atomic fraction in Au/rod-CeO_2 and Pt/rod-CeO_2 decreases to 4−12% only. Clearly, the density of oxygen vacancies in the surface region of rod-CeO_2 of M/rod-CeO_2 is lower than that of the surface region of internal concave walls of the CeO_2 pore of M@mp-CeO_2 during WGS catalysis. A similar difference was observed between Pd@mp-CeO_2 and Pd/rod-CeO_2 and between Cu@mp-CeO_2 and Cu/rod-CeO_2 (Figures S7−S10).

Typically, H_2O dissociates on oxygen vacancies of bifunctional WGS catalysts (metal nanoclusters supported on reducible oxides or clusters of reducible oxide supported on the metal surface).[16] Higher adsorption energy of OH groups on oxygen vacancies means a stronger adsorption of OH groups during catalysis from the point of view of thermodynamics. Thus, a lower density of oxygen vacancies could be observed if there is a stronger adsorption of OH groups. The reason that OH groups are favorably adsorbed on oxygen vacancies of a rod-CeO_2 instead of a concave internal surface of CeO_2 pores of mp-CeO_2 and the adsorption energy of a OH group on an oxygen vacancy of a rod-CeO_2 is stronger is a larger repulsion between adjacent OH groups on the concave internal surface resulting from the limited space of the concave internal surface. This difference is schematically shown in Figure S12. The concave internal surface increases repulsion of the neighboring adsorbates. The increase of repulsion of OH groups on the internal concave
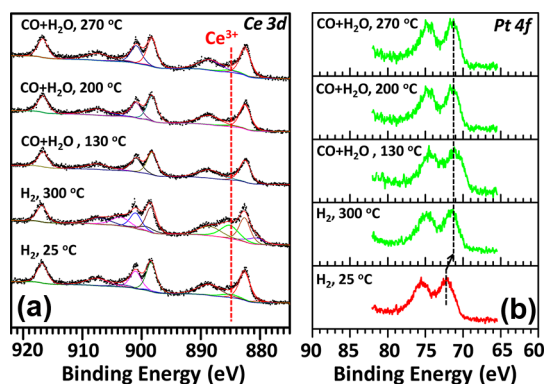

Figure 8. Photoemission features of (a) Ce 3d and (b) Pt 4f of Pt/rod-CeO_2 under reaction conditions studied with AP-XPS. $P_{CO} = 0.3$ Torr, $P_{H_2O} = 1.2$ Torr, $P_{H_2} = 1$ Torr. Reaction temperatures are given in the figure.
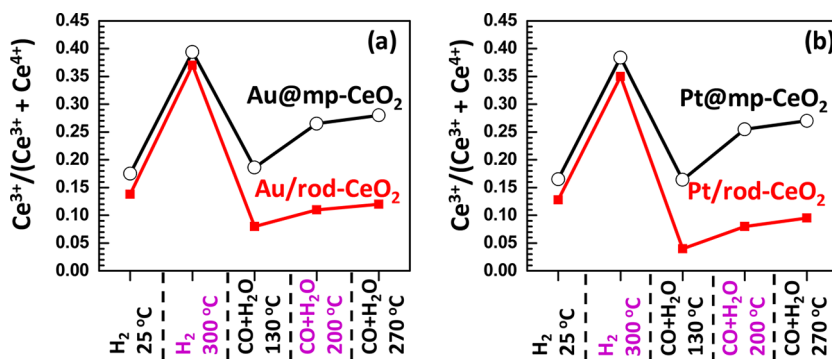

Figure 9. Evolution of atomic fractions of Ce^{3+} of Au@mp-CeO_2 and Au/rod-CeO_2 (a) and Pt@mp-CeO_2 and Pt/rod-CeO_2 (b) during WGS.

surface is an opposite effect to the decrease of repulsion of adsorbates through formation of an open surface of nanoclusters *via* breaking a stepped surface Pt(557).[26,27]

XPS studies show that both gold and platinum of metal nanoclusters *in* *mp*-CeO$_2$ or *on* rod-CeO$_2$ before reactions exist in an oxidized chemical state instead of a metal state (Figures 5—8). They were reduced to the metallic state upon the pretreatment in H$_2$ at 300 °C. Notably, AP-XPS studies showed the binding energies of Au 4f and Pt 4f remain in a metallic state under WGS conditions (Figures 5—8). As described in the Methods section, the surface charging is in the range of about 0.2 eV or less. In addition, the difference in surface charging between a catalyst in H$_2$ and one in CO + H$_2$O is extremely small. Thus, the downshift of binding energy of Au 4f (or Pt 4f) in the WGS condition in contrast to that before any reactions clearly indicated a change of oxidation state of gold (or platinum) in these catalysts during catalysis. Thus, the *in situ* studies using AP-XPS suggested the metallic state of Au and Pt encapsulated in *mp*-CeO$_2$ or on rod-CeO$_2$ during WGS catalysis. The metallic state of Pd and Cu was also suggested for Pd@*mp*-CeO$_2$ (Figure S7), Pd/rod-CeO$_2$ (Figure S8), Cu@*mp*-CeO$_2$ (Figure S9), and Cu/rod-CeO$_2$ (Figure S10) under WGS reaction conditions.

These parallel studies of M@*mp*-CeO$_2$ and M/rod-CeO$_2$ catalysts show a higher density of oxygen vacancies on the surface of the internal concave surface of CeO$_2$ pores of *mp*-CeO$_2$ during catalysis (Figure 9). In addition, AP-XPS studies suggested the metallic state of Au, Pt, Pd, and Cu nanoparticles encapsulated in *mp*-CeO$_2$ during catalysis. On the basis of these *in situ* studies, the difference in activation energy is related to the different surface chemistry of *mp*-CeO$_2$ of M@*mp*-CeO$_2$ and rod-CeO$_2$ of M/rod-CeO$_2$ under the same reaction condition. The high concentration of oxygen vacancies on the internal wall of *mp*-CeO$_2$ suggests low adsorption energy of the OH group on the internal concave wall of *mp*-CeO$_2$ during catalysis, which could contribute to the lower activation energy of WGS on M@*mp*-CeO$_2$ compared to M/rod-CeO$_2$.

SUMMARY

Au, Pt, Pd, and Cu nanoclusters encapsulated in *mp*-CeO$_2$ were synthesized through a template of SBA-15. WGS performed at the interface of Au, Pt, Pd, and Cu nanoclusters and the concave surface of the internal walls of CeO$_2$ pore of *mp*-CeO$_2$ exhibits lower activation energies than metal nanoclusters supported on flat surfaces of rod-CeO$_2$. The surface chemistries of metal nanoclusters and CeO$_2$ during WGS were studied by using AP-XPS. Our AP-XPS studies identified the metallic state of Au, Pt, Pd, and Cu nanoclusters of these catalysts *during* WGS. The measurements of oxygen vacancies of *mp*-CeO$_2$ of M@*mp*-CeO$_2$ and rod-CeO$_2$ of M/rod-CeO$_2$ during WGS suggested a correlation between the surface chemistry of the concave, surface of the internal walls of the CeO$_2$ pore of *mp*-CeO$_2$, and low activation energy of M@*mp*-CeO$_2$ in contrast to those of M/rod-CeO$_2$.

METHODS

Synthesis of M@*mp*-CeO$_2$ involved three steps (synthesis of SBA-15, formation of *mp*-CeO$_2$ using the SBA-15 template, and encapsulation of metal nanoclusters into channels of *mp*-CeO$_2$), as schematically shown in Figure 10. It is different from the deposition—precipitation method for formation of metal nanoparticles *on* *mp*-CeO$_2$ particles[39] since the metal nanoclusters in our work are encapsulated *in* the channel of *mp*-CeO$_2$.

The *mp*-CeO$_2$ was prepared by the hard-template method. SBA-15 was used as the template.[41] The SBA-15 was synthesized by following the method reported in the literature.[3] Typically, 10.2 g of Pluronic P123 (EO$_{20}$PO$_{70}$EO$_{20}$ (M_{av} = 5800) Aldrich) was dissolved into 329 mL of deionized water and 62 mL of 37% HCl solution. Then, 22.44 g of tetraethylorthosilicate (TEOS) (Aldrich) was added to the acid solution and was subsequently stirred at 35 °C for 20 h. Then the solution was crystallized at 80 °C for 10 h. The crystallization yielded white precipitates, which were collected by filtration. The white precipitates were further calcined at 550 °C for 3 h to remove organic surfactants. The as-obtained product is SBA-15 (Figure 10a), which is used as the hard template for preparation of *mp*-CeO$_2$.

In the synthesis of *mp*-CeO$_2$, 9.4 g of Ce(NO$_3$)$_3$·6H$_2$O was dissolved into 20 mL of ethanol (Aldrich). Then, 2 g of SBA-15 was added to the ethanol solution kept at 35 °C with mild stirring to evaporate the ethanol. After evaporation, the mixture was calcined at 300 °C for 3 h to transform the Ce(NO$_3$)$_3$ to CeO$_2$. Afterward, the impregnation process was repeated by using 3.3 g of Ce(NO$_3$)$_3$·6H$_2$O in 20 mL of ethanol. This product was calcined at 550 °C for 3 h to form *mp*-CeO$_2$/SBA (Figure 10b). The silica in the *mp*-CeO$_2$/SBA was removed by 1 M NaOH solution for three times to get *mp*-CeO$_2$ (Figure 10c), which was dried at 110 °C overnight. Figure 10 schematically represents the

process of synthesizing *mp*-CeO$_2$.[41] The crystallization of *mp*-CeO$_2$ was confirmed with SEM and XRD (Figure 1).

For the synthesis of rod-CeO$_2$, a hydrothermal method was used:[42] 0.868 g of Ce(NO$_3$)$_3$·6H$_2$O was dissolved in 5 mL of deionized water. Then 35 mL of 6 M NaOH was added to the solution. The as-obtained mixture was transferred and sealed into a Teflon-lined autoclave and kept at 100 °C for 24 h. The precipitate was collected by filtration and calcination at 400 °C for 4 h, and the final product was denoted as rod-CeO$_2$.

The metal nanoclusters were formed on the internal surface of the wall of channels of *mp*-CeO$_2$ or on the external surface of rod-CeO$_2$ through impregnation. A certain amount of precursors of these metal nanoclusters was dissolved in ethanol, and 0.5 g of *mp*-CeO$_2$ or rod-CeO$_2$ was added to the solution. HAuCl$_4$·3H$_2$O (Aldrich), H$_2$PtCl$_6$·6H$_2$O (Aldrich), PdCl$_2$ (Aldrich), and Cu(NO$_3$)$_2$·2.5H$_2$O (Aldrich) were precursors of impregnation for formation of Au, Pt, Pd, and Cu metal nanoclusters in CeO$_2$ pores of *mp*-CeO$_2$ and on rod-CeO$_2$. The loading of each metal on CeO$_2$ is 2.5 wt %. Precursor is dissolved in ethanol. The ethanol was gradually evaporated at 35 °C, then the solids were calcined at ~450 °C for 3 h. Size of metal nanoclusters encapsulated in *mp*-CeO$_2$ is similar to those on rod-CeO$_2$ (see Table 1).

Powder XRD patterns of catalysts were collected on a Bruker D8 Avance diffractometer using Cu Kα radiation (λ = 1.54056 Å). Structure and morphology of catalysts synthesized above were characterized with SEM (FEI Magellan XHR 400) at 15 kV. Size, shape, and lattice fringe of the catalysts upon a pretreatment in H$_2$ were identified with Titan TEM (FEI Titan 80—300, 300 kV FEG TEM with point resolution 0.2 Å).

The catalytic activity of the WGS was tested in a fixed-bed microflow reactor at atmospheric pressure. Fifty milligrams of
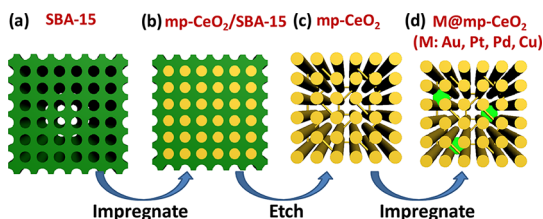
(a) SBA-15   **(b)** mp-CeO$_2$/SBA-15   **(c)** mp-CeO$_2$ **(d)** M@mp-CeO$_2$ (M: Au, Pt, Pd, Cu)

Impregnate   Etch   Impregnate

Figure 10. Process of the synthesis of metal nanoclusters encapsulated in pores of mp-CeO$_2$ (M@mp-CeO$_2$). **The green balls in (d) represent metal nanoclusters encapsulated in mp-CeO$_2$.**

catalyst was used for each test. Before catalytic tests, WGS catalysts were reduced *in situ* under a flow of 5% H$_2$/95%Ar (50 mL min^{-1}) at 300 °C for 45 min. After the pretreatment, the catalysts were cooled to room temperature in 5% H$_2$/Ar (50 mL min^{-1}). Reactant composition was 5.6% CO and 22.44% H$_2$O with Ar balance. Water was brought into the reactor by a high-performance liquid chromatography pump. The total flow rate of the reactant gas is 50 mL min^{-1}. This catalytic condition kept the conversion lower than 5% for kinetic studies. The effluent gas was analyzed by a gas chromatograph (HP 5890 II). The CO conversions were calculated using following equations:

$$X\% = \frac{A_{t_0} - A_t}{A_{t_0}}$$

Here A is the peak area of CO from the GC; t_0 is the sampling time before the WGS reaction, and t is after the WGS reaction. Plotting of ln X as a function of $1000/T$ gave the slope, from which activation energies E_a were calculated.

In situ studies of metal nanoclusters encapsulated in mp-CeO$_2$ and supported on rod-CeO$_2$ were performed by using the ambient-pressure XPS using a benchtop X-ray source, mono-chromated Al Kα. This system includes three sections: ambient-pressure XPS, sample preparation chamber, and 20 bar reaction cell (not used for this work). Figure S1 shows photos of this system in the Tao group. Reactant gas can flow through the catalysts during XPS analysis. During catalysis, samples are heated conductively through an external heating source. This external heating excluded the possibility of any catalytic reactions that a filament may induce. The test of this whole AP-XPS system showed that it can examine a silver thin-film sample at a pressure up to 25−50 Torr. The resolution of Ag 3d$_{5/2}$ in 25 Torr N$_2$ is 0.46 or 0.85 eV corresponding to a pass energy of 5 or 40 eV, respectively. The reasonable count rate of ~6000 at a pressure as high as 25−50 Torr N$_2$ suggests the capability of *in situ* studies at such a relatively high pressure (Figure S2). The acquisition time of Ag 3d (Figure S2) within a few minutes exceeded the possibility of reducing sample surfaces due to a long-time X-ray irradiation. Detailed information on the AP-XPS system and its functions can be found in Supporting Information and literature.[43]

To avoid surface charging, we do not use a silicon wafer to load catalysts for AP-XPS studies. Here, a Au or Ag single crystal is used as a substrate for AP-XPS studies. A Au single crystal was used as a substrate of Pt@mp-CeO$_2$, Pt/rod-CeO$_2$, Cu@mp-CeO$_2$, and Cu/rod-CeO$_2$ samples for AP-XPS studies. Due to the overlap of the photoemission features of Au 3d and Pd 3d, a Ag single crystal was used as a substrate of Au@mp-CeO$_2$, Au/rod-CeO$_2$, Pd@mp-CeO$_2$, and Pd/rod-CeO$_2$. Catalysts were dispersed in ethanol. Samples of AP-XPS studies were prepared by drop-casting the ethanol solution containing the dispersed WGS nanoparticle catalyst onto the Au or Ag single-crystal surface. Natural evaporation of ethanol in ambient condition at 50 °C was performed before loading a sample into the UHV chamber and then transferred to the AP-XPS reaction cell.

To minimize potential surface charging during data acquisition, coverage of nanocatalysts on the surface of Au or Ag is kept at a level lower than 40%. The charging is in the range of 0.2 eV, which is nearly within error of binding energy measurements of XPS using Al Kα.

It is well-known that the sampling depth of AP-XPS is very similar to vacuum XPS in the range of a few nanometers. To

exclude the potential contribution of metal nanoclusters potentially formed on the external surface of a mp-CeO$_2$ particle to the photoemission feature, surface layers (about 10 nm) were removed through Ar sputtering. The removal of a certain thickness can be confirmed with electron microscopy techniques. To confirm the removal of nanoclusters potentially formed on the surface of mp-CeO$_2$ particles, a longer sputtering was typically performed. There was no change of photoemission features and intensities of core levels from metal nanoclusters upon a longer sputtering. So, we exclude the possibility of contribution of information from nanoclusters potentially formed on the external surface of mp-CeO$_2$ particles. Then, the sputtered surfaces were used for XPS studies. Figure S3 schematically presents the method described above.

The AP-XPS studies of M@mp-CeO$_2$ using AP-XPS were performed at temperatures of 130, 200, and 270 °C in a gaseous environment of 0.3 Torr CO and 1.2 Torr H$_2$O, or 1 Torr of H$_2$. Argon ion sputtering was used to remove any potential metal nanoparticles on the external surface of mp-CeO$_2$ particles to make sure the photoemission feature of metal nanoclusters is solely contributed from the nanoclusters encapsulated in mp-CeO$_2$. In addition, TEM studies of the edge of mp-CeO$_2$ by tilting the edge of M@mp-CeO$_2$ during TEM examination did not find metal nanoparticles on the external surface of M@mp-CeO$_2$.

Deconvolution of all Ce 3d spectra was done with Casa always using the same set of parameters. The positions, widths, and shapes of 10 peaks for each Ce 3d spectrum were fixed so that the calculated atomic ratios of Ce^{3+} to a total of Ce^{3+} and Ce^{4+} are comparable. Each of these Ce 3d spectra was deconvoluted into 10 peaks: ν_o, ν, ν', ν'', ν''', μ_o, μ, μ', μ'', and μ''' from low binding energy to high binding energy. The six peaks corresponding to three pairs of spin−orbital doublets (ν, ν'', ν''', μ, μ'', and μ''') are contributed from Ce^{4+}, resulting from different Ce 4f occupancies in the final state.[44] The ν_o, ν', μ_o, and μ' are assigned to Ce^{3+}.[34] The positions of the six peaks of Ce^{4+} and four peaks of Ce^{3+} referred to XPS studies of CeO$_2$ and Ce$_2$O$_3$ samples reported in the literature[40] and from our recent studies of pure oxides. The measured nominal binding energies of μ''' of Ce^{4+} in our XPS studies are very close to that reported in literature[40] within the error of measurements, which confirmed the minimized surface charging under reaction conditions in our experiments.

Conflict of Interest: The authors declare no competing financial interest.

Supporting Information Available: Characterization of catalysts during catalysis using in-house ambient-pressure XPS, XRD, and TEM of rod-CeO$_2$ and other catalysts, TEM images of M@CeO$_2$ and M/rod-CeO$_2$, their photoemission features studied using AP-XPS, and structural model illustrating the difference between external surface of rod-CeO$_2$ and concave internal surface of mp-CeO$_2$ are available. This material is available free of charge *via* the Internet at http://pubs.acs.org.

REFERENCES AND NOTES

1. Kresge, C. T.; Leonowicz, M. E.; Roth, W. J.; Vartuli, J. C.; Beck, J. S. Ordered Mesoporous Molecular Sieves Synthesized by a Liquid-Crystal Template Mechanism. *Nature* **1992**, *359*, 710–712.

2. Beck, J. S.; Vartuli, J. C.; Roth, W. J.; Leonowicz, M. E.; Kresge, C. T.; Schmitt, K. D.; Chu, C. T. W.; Olson, D. H.; Sheppard, E. W. A New Family of Mesoporous Molecular Sieves Prepared with Liquid Crystal Templates. *J. Am. Chem. Soc.* **1992**, *114*, 10834–10843.

3. Zhao, D.; Feng, J.; Huo, Q.; Melosh, N.; Fredrickson, G. H.; Chmelka, B. F.; Stucky, G. D. Triblock Copolymer Syntheses of Mesoporous Silica with Periodic 50 to 300 Angstrom Pores. *Science* **1998**, *279*, 548–552.

4. Yang, P.; Zhao, D.; Margolese, D. I.; Chmelka, B. F.; Stucky, G. D. Generalized Syntheses of Large-Pore Mesoporous Metal Oxides with Semicrystalline Frameworks. *Nature* **1998**, *396*, 152–155.

5. Joo, S. H.; Choi, S. J.; Oh, I.; Kwak, J.; Liu, Z.; Terasaki, O.; Ryoo, R. Ordered Nanoporous Arrays of Carbon Supporting High Sispersions of Platinum Nanoparticles. *Nature* **2001**, *412*, 169–172.

6. Li, H.; Eddaoudi, M.; O'Keeffe, M.; Yaghi, O. M. Design and Synthesis of an Exceptionally Stable and Highly Porous Metal-Organic Framework. *Nature* **1999**, *402*, 276–279.

7. Feng, X.; Fryxell, G. E.; Wang, L.-Q.; Kim, A. Y.; Liu, J.; Kemner, K. M. Functionalized Monolayers on Ordered Mesoporous Supports. *Science* **1997**, *276*, 923–926.

8. Rosi, N. L.; Eckert, J.; Eddaoudi, M.; Vodak, D. T.; Kim, J.; O'Keeffe, M.; Yaghi, O. M. Hydrogen Storage in Microporous Metal-Organic Frameworks. *Science* **2003**, *300*, 1127–1129.

9. Thomas, J. M.; Raja, R. Exploiting Nanospace for Asymmetric Catalysis: Confinement of Immobilized, Single-Site Chiral Catalysts Enhances Enantioselectivity. *Acc. Chem. Res.* **2008**, *41*, 708–720.

10. De Vos, D. E.; Dams, M.; Sels, B. F.; Jacobs, P. A. Ordered Mesoporous and Microporous Molecular Sieves Functionalized with Transition Metal Complexes as Catalysts for Selective Organic Transformations. *Chem. Rev.* **2002**, *102*, 3615–3640.

11. Corma, A. From Microporous to Mesoporous Molecular Sieve Materials and Their Use in Catalysis. *Chem. Rev.* **1997**, *97*, 2373–2420.

12. Zhang, H.; Zhang, Y.; Li, C. Enantioselective Epoxidation of Unfunctionalized Olefins Catalyzed by the Mn(Salen) Catalysts Immobilized in the Nanopores of Mesoporous Materials. *J. Catal.* **2006**, *238*, 369–381.

13. Pan, X.; Fan, Z.; Chen, W.; Ding, Y.; Luo, H.; Bao, X. Enhanced Ethanol Production inside Carbon-Nanotube Reactors Containing Catalytic Particles. *Nat. Mater.* **2007**, *6*, 507–511.

14. Chen, W.; Pan, X.; Bao, X. Tuning of Redox Properties of Iron and Iron Oxides *via* Encapsulation within Carbon Nanotubes. *J. Am. Chem. Soc.* **2007**, *129*, 7421–7426.

15. Chen, W.; Fan, Z.; Pan, X.; Bao, X. Effect of Confinement in Carbon Nanotubes on the Activity of Fischer−Tropsch Iron Catalyst. *J. Am. Chem. Soc.* **2008**, *130*, 9414–9419.

16. Rodriguez, J. A.; Ma, S.; Liu, P.; Hrbek, J.; Evans, J.; Perez, M. Activity Of CeO_x and TiO_x Nanoparticles Grown on Au(111) in the Water-Gas Shift Reaction. *Science* **2007**, *318*, 1757–1760.

17. Fu, Q.; Saltsburg, H.; Flytzani-Stephanopoulos, M. Active Nonmetallic Au and Pt Species on Ceria-Based Water-Gas Shift Catalysts. *Science* **2003**, *301*, 935–938.

18. Zhang, C. J.; Michaelides, A.; King, D. A.; Jenkins, S. J. Positive Charge States and Possible Polymorphism of Gold Nanoclusters on Reduced Ceria. *J. Am. Chem. Soc.* **2010**, *132*, 2175–2182.

19. Deng, W.; Frenkel, A. I.; Si, R.; Flytzani-Stephanopoulos, M. Reaction-Relevant Gold Structures in the Low Temperature Water-Gas Shift Reaction on $Au-CeO_2$. *J. Phys. Chem. C* **2008**, *112*, 12834–12840.

20. Goguet, A.; Burch, R.; Chen, Y.; Hardacre, C.; Hu, P.; Joyner, R. W.; Meunier, F. C.; Mun, B. S.; Thompsett, A.; Tibiletti, D. Deactivation Mechanism of a $Au/CeZrO_4$ Catalyst during a Low-Temperature Water Gas Shift Reaction. *J. Phys. Chem. C* **2007**, *111*, 16927–16933.

21. Rodriguez, J. A.; Liu, P.; Hrbek, J.; Evans, J.; Pérez, M. Water Gas Shift Reaction on Cu and Au Nanoparticles Supported on CeO_2(111) and ZnO(0001): Intrinsic Activity and Importance of Support Interactions. *Angew. Chem., Int. Ed.* **2007**, *46*, 1329–1332.

22. Rodriguez, J. A.; Hanson, J. C.; Wen, W.; Wang, X.; Brito, J. L.; Martinez-Arias, A.; Fernandez-Garcia, M. *In Situ* Characterization of Water-Gas Shift Catalysts Using Time-Resolved X-ray Diffraction. *Catal. Today* **2009**, *145*, 188–194.

23. Rodriguez, J. A.; Hrbek, J. Inverse Oxide/Metal Catalysts: A Versatile Approach for Activity Tests and Mechanistic Studies. *Surf. Sci.* **2010**, *604*, 241–244.

24. Park, J. B.; Graciani, J.; Evans, J.; Stacchiola, D.; Ma, S.; Liu, P.; Nambu, A.; Fernandez Sanz, J.; Hrbek, J.; Rodriguez, J. A. High Catalytic Activity of $Au/CeO_x/TiO_2$(110) Controlled by the Nature of the Mixed-Metal Oxide at the Nanometer Level. *Proc. Natl. Acad. Sci. U.S.A.* **2009**, *106*, 4975–4980.

25. Zhai, Y.; Pierre, D.; Si, R.; Deng, W.; Ferrin, P.; Nilekar, A. U.; Peng, G.; Herron, J. A.; Bell, D. C.; Saltsburg, H.; et al. Alkali-Stabilized $Pt-OH_x$ Species Catalyze Low-Temperature Water-Gas Shift Reactions. *Science* **2010**, *329*, 1633–1636.

26. Tao, F.; Salmeron, M. *In Situ* Studies of Chemistry and Structure of Materials in Reactive Environments. *Science* **2011**, *331*, 171–174.

27. Tao, F.; Dag, S.; Wang, L.-W.; Liu, Z.; Butcher, D. R.; Bluhm, H.; Salmeron, M.; Somorjai, G. A. Break-Up of Stepped Platinum Catalyst Surfaces by High CO Coverage. *Science* **2010**, *327*, 850–853.

28. Tao, F.; Grass, M. E.; Zhang, Y.; Butcher, D. R.; Renzas, J. R.; Liu, Z.; Chung, J. Y.; Mun, B. S.; Salmeron, M.; Somorjai, G. A. Reaction-Driven Restructuring of Rh−Pd and Pt−Pd Core−Shell Nanoparticles. *Science* **2008**, *322*, 932–934.

29. Wen, C.; Liu, Y.; Tao, F. Integration of Surface Science, Nanoscience, and Catalysis. *Pure Appl. Chem.* **2011**, *83*, 243–252.

30. Sun, B.; Qiao, M.; Fan, K.; Ulrich, J.; Tao, F. Fischer−Tropsch Synthesis over Molecular Sieve Supported Catalysts. *ChemCatChem* **2011**, *3*, 542–550.

31. Ogletree, D. F.; Bluhm, H.; Lebedev, G.; Fadley, C. S.; Hussain, Z.; Salmeron, M. A Differentially Pumped Electrostatic Lens System for Photoemission Studies in the Millibar Range. *Rev. Sci. Instrum.* **2002**, *73*, 3872–3877.

32. Salmeron, M.; Schlogl, R. Ambient Pressure Photoelectron Spectroscopy: A New Tool for Surface Science and Nanotechnology. *Surf. Sci. Rep.* **2008**, *63*, 169–199.

33. Grass, M. E.; Karlsson, P. G.; Aksoy, F.; Lundqvist, M.; Wannberg, B.; Mun, B. S.; Hussain, Z.; Liu, Z. New Ambient Pressure Photoemission Endstation at Advanced Light Source Beamline 9.3.2. *Rev. Sci. Instrum.* **2010**, *81*, 053106.

34. Si, R.; Flytzani-Stephanopoulos, M. Shape and Crystal-Plane Effects of Nanoscale Ceria on the Activity of Au-CeO_2 Catalysts for the Water-Gas Shift Reaction. *Angew. Chem., Int. Ed.* **2008**, *47*, 2884–2887.

35. Panagiotopoulou, P.; Kondarides, D. I. Effect of the Nature of the Support on the Catalytic Performance of Noble Metal Catalysts for the Water-Gas Shift Reaction. *Catal. Today* **2006**, *112*, 49–52.

36. Grass, M.; Rioux, R.; Somorjai, G. Dependence of Gas-Phase Crotonaldehyde Hydrogenation Selectivity and Activity on the Size of Pt Nanoparticles (1.7−7.1 nm) Supported on SBA-15. *Catal. Lett.* **2009**, *128*, 1–8.

37. Longo, A.; Liotta, L. F.; Pantaleo, G.; Giannici, F.; Venezia, A. M.; Martorana, A. Structure of the Metal-Support Interface and Oxidation State of Gold Nanoparticles Supported on Ceria. *J. Phys. Chem. C* **2012**, *116*, 2960–2966.

38. Dholabhai, P. P.; Adams, J. B.; Crozier, P.; Sharma, R. Oxygen Vacancy Migration in Ceria and Pr-Doped Ceria: A DFT Plus U Study. *J. Chem. Phys.* **2010**, *132*, 094104.

39. Yuan, Z. Y.; Idakiev, V.; Vantomme, A.; Tabakova, T.; Ren, T. Z.; Su, B. L. Mesoporous and Nanostructured CeO_2 as Supports of Nano-Sized Gold Catalysts for Low-Temperature Water-Gas Shift Reaction. *Catal. Today* **2008**, *131*, 203–210.

40. Mullins, D. R.; Overbury, S. H.; Huntley, D. R. Electron Spectroscopy of Single Crystal and Polycrystalline Cerium Oxide Surfaces. *Surf. Sci.* **1998**, *409*, 307–319.

41. Lu, A. H.; Schüth, F. Nanocasting: A Versatile Strategy for Creating Nanostructured Porous Materials. *Adv. Mater.* **2006**, *18*, 1793–1805.

42. Si, R.; Flytzani-Stephanopoulos, M. Shape and Crystal-Plane Effects of Nanoscale Ceria on the Activity of Au-CeO_2 Catalysts for the Water−Gas Shift Reaction. *Angew. Chem., Int. Ed.* **2008**, *47*, 2884–2887.

43. Tao, F. Design of an In-House Ambient Pressure XPS Using a Bench-Top X-ray Source and Surface Chemistry of Ceria under Reaction Conditions. *Chem. Commun.* **2012**, *48*, 3812–3814.

44. Elfallah, J.; Boujana, S.; Dexpert, H.; Kiennemann, A.; Majerus, J.; Touret, O.; Villain, F.; Lenormand, F. Redox Processes of Pure Ceria and on Rh/CeO_2 Catalysts Monitoried by X-ray Absorption (Fast Acquistion Mode). *J. Phys. Chem.* **1994**, *98*, 5522–5533.